

Northumbria Research Link

Citation: Zhou, Kai, Chen, Wenge, Yang, Yana, Li, Rong, Dong, Longlong and Fu, Yong Qing (2022) Microstructure and mechanical behavior of porous tungsten skeletons synthesized by selected laser melting. International Journal of Refractory Metals and Hard Materials, 103. p. 105769. ISSN 0263-4368

Published by: Elsevier

URL: <https://doi.org/10.1016/j.ijrmhm.2021.105769>
<<https://doi.org/10.1016/j.ijrmhm.2021.105769>>

This version was downloaded from Northumbria Research Link:
<https://nrl.northumbria.ac.uk/id/eprint/48053/>

Northumbria University has developed Northumbria Research Link (NRL) to enable users to access the University's research output. Copyright © and moral rights for items on NRL are retained by the individual author(s) and/or other copyright owners. Single copies of full items can be reproduced, displayed or performed, and given to third parties in any format or medium for personal research or study, educational, or not-for-profit purposes without prior permission or charge, provided the authors, title and full bibliographic details are given, as well as a hyperlink and/or URL to the original metadata page. The content must not be changed in any way. Full items must not be sold commercially in any format or medium without formal permission of the copyright holder. The full policy is available online: <http://nrl.northumbria.ac.uk/policies.html>

This document may differ from the final, published version of the research and has been made available online in accordance with publisher policies. To read and/or cite from the published version of the research, please visit the publisher's website (a subscription may be required.)

Microstructure and mechanical behavior of porous tungsten skeletons synthesized by selected laser melting

Kai Zhou¹, Wenge Chen^{1*}, Yana Yang¹, Rong Li¹, Longlong Dong², Yong-Qing Fu^{3*}

¹ School of Materials Science and Engineering, Xi'an University of Technology, Xi'an, Shaanxi, 710048, P.R. China

² Advanced Materials Research Central, Northwest Institute for Nonferrous Metal Research, Xi'an, 710016, PR China

³ Faculty of Engineering and Environment, Northumbria University, Newcastle upon Tyne, NE1 8ST, UK

Abstract:

Because of its high ductile-brittle transition temperature, tungsten (W) is normally alloyed with other metal elements in order to obtain high fracture strength, excellent thermal and electrical properties for industrial applications. For tungsten samples sintered using the conventional powder metallurgy methods, bonding among tungsten particles is normally through sintered necking process, thus without providing a good metallurgical bonding strength. In this paper, we proposed to apply additive manufacture methodology to synthesize two types of porous tungsten skeleton structures, honeycomb (65% porosity) and square skeleton (80% porosity), using a selective laser melting (SLM) method. Results showed that for both these skeleton structures, grains in the XY plane showed an equiaxed crystal appearance, whereas those in the YZ/XZ plane showed columnar patterns parallel to the Z axis. The measured porosities for these two types of skeletons were 52 vol.% and 68 vol.%, and their compressive strength values were 256 MPa and 149 MPa, respectively. Both their compressive strengths and hardness showed anisotropic behaviors, with their highest values along the direction of Z axis. Results also showed that fracture morphology and mechanisms of these skeletons under compression were quite different when they were compressed along different directions, mainly due to the formed columnar crystals of the skeletons along the Z axis. Fracture morphology along the Z axis showed transgranular fracture and tearing features, whereas those along X axis showed only intergranular fracture features.

Keywords: Selective Laser Melting, Porous Tungsten, Microstructure, Fracture Mechanism

¹ Corresponding authors: Professor Wenge Chen; Prof. Richard Y.Q.Fu.
E-mail: wgchen001@263.net (W.G. Chen), richard.fu@northumbria.ac.uk (Richard Y.Q. Fu)

1 **1. Introduction**

2

3 Tungsten, one of the most important refractory metals, has many outstanding properties such
4 as high melting point (3420°C), high hardness, excellent anti-ablation property and low tritium
5 retention effect [1]. Owing to these merits, it has been the prime candidate material for rocket
6 nozzles or plasma facing material in nuclear fusion [2]. It has also been applied as a matrix for
7 alloying with other metals such as Cu, Fe or Ag, which have been successfully applied as the
8 high-temperature components for the diverter and electrical contact [3]. The conventional methods
9 used for fabricating tungsten matrix composites include powder metallurgy [4], spark plasma
10 sintering [5] and hot isostatic pressing [6]. However, the tungsten matrix with a skeleton structure
11 in composites prepared by these methods often showed poor bonding because these W particles are
12 simply consolidated through sintered necking process, thus it is hard to achieve a solid structure
13 with a high strength.

14 It is well-known that modification of the interconnected structures could improve the
15 mechanical and functional properties of skeletons [7]. Additive manufacture is regarded as an
16 effective method to fabricate tungsten skeletons with good metallurgical bonding. Selective laser
17 melting (SLM), one of the additive manufacture methods, has merits of design freedom and
18 net-shape forming capability, and has been used to manufacture highly porous refractory metals
19 such as tungsten [8] and tantalum [9,10]. However, as it is well-known, pure tungsten is prone to
20 cracking during additive manufacturing, because of grain boundary oxidation [11] and large
21 residual stress caused by its high ductile brittle transition temperature.

22 Up to now, there are few studies of the porous tungsten fabricated by using SLM, and a lot of
23 work is needed to understand the relationships among microstructures, mechanical properties and
24 process parameters. Recently pure W samples with a density of 98.51% have been produced by
25 SLM using spherical powders [12]. Hu et.al. [13] fabricated pure tungsten using the SLM and
26 achieved a high density of $98.3\pm 0.3\%$. They reported that the cracking of tungsten is due to the
27 existence of tungsten oxide impurities at grain boundaries. Guo et.al. [14] studied the volumetric
28 energy densities and their relationship with mechanical properties of tungsten sample prepared by
29 the SLM, and reported that the fracture was brittle with an intergranular mode. Wen et.al. [15]
30 manufactured high-density pure tungsten (98.71%) by SLM, and they found that the axial splitting
31 was the main fracture feature and the crack appeared occurring at the grain boundaries. However,
32 highly porous tungsten skeletons fabricated by SLM and their fracture behaviors and mechanisms
33 have never been reported as far as we have searched in literature.

34 This paper used the SLM method to fabricate highly porous tungsten but high strength
35 skeleton structures with two different shapes, i.e., square and honey-comb. The isotropic and

1 anisotropic microstructures and mechanical properties of the sintered W skeletons were
2 systematically studied, and the compressive fracture mechanisms of these two skeletons are
3 systematically studied.

4 **2. Experimental methods**

5 Spherical tungsten powders with an average particle size of 15-53 μm were obtained from
6 Institute of Materials and Processing, Guangdong Academy of Sciences. Their compositions are
7 listed in Table 1. Two types of porous tungsten skeletons were designed as shown in Fig. 1(a), e.g.,
8 honey comb (65% porosity) and square (80% porosity). Their designed structures and manufacture
9 processes are illustrated in Fig. 1. The porous tungsten skeletons were synthesized using an EOS
10 M290 SLM system equipped with a Yb fiber-laser (with a beam diameter of 100 μm and a
11 maximum output power of 400 W). During the experiments, laser power and scanning speed were
12 150 W and 350 mm/s, respectively. The scanning path of laser beam was a zigzag pattern with 67°
13 rotation between the adjacent scanning layers. For each path, the layer thickness and hatch
14 distance were 25 μm and 80 μm , respectively. All the experiments were conducted in an Ar
15 atmosphere, and all the samples were synthesized on a pure tungsten plate. For compression tests,
16 the compressive strength was obtained using a material testing machine (HT-2402) at room
17 temperature, and the samples have a height to diameter ratio of 1~2. The compression directions
18 were chosen along Z axis (building direction, BD) and X axis (perpendicular to the building
19 direction, PBD), respectively.

20 Microstructure of the W skeleton was observed using an inverted metallographic microscope
21 (GX71, OLYMPUS, Japan), after the samples were etched with a chemical reagent of HF: HNO₃
22 (3:1 in a volume ratio). An X-ray diffractometer (XRD-7000, Shimadzu, Japan) with Cu K α
23 radiation at 40 kV and 40 mA was used to analyze the crystalline structures of the samples. The
24 scanning speed was 2°/min and the scanning range of 2 θ was 10-90° with a step size of 0.02°.
25 Surface morphology and compression fracture morphology were observed using a scanning
26 electron microscope (SEM, TESCAN VEGA3 XMU, Czech Republic). Sample were sectioned
27 and polished before the Vickers hardness measurements.

28 The Archimedes method (equation 1) was used to measure the specimen's density, and the
29 porosity (k) of skeletons was calculated using equation 2.

$$\rho = \rho_{\text{water}} \cdot \frac{m_0}{m_0 - m_1} \quad (1)$$

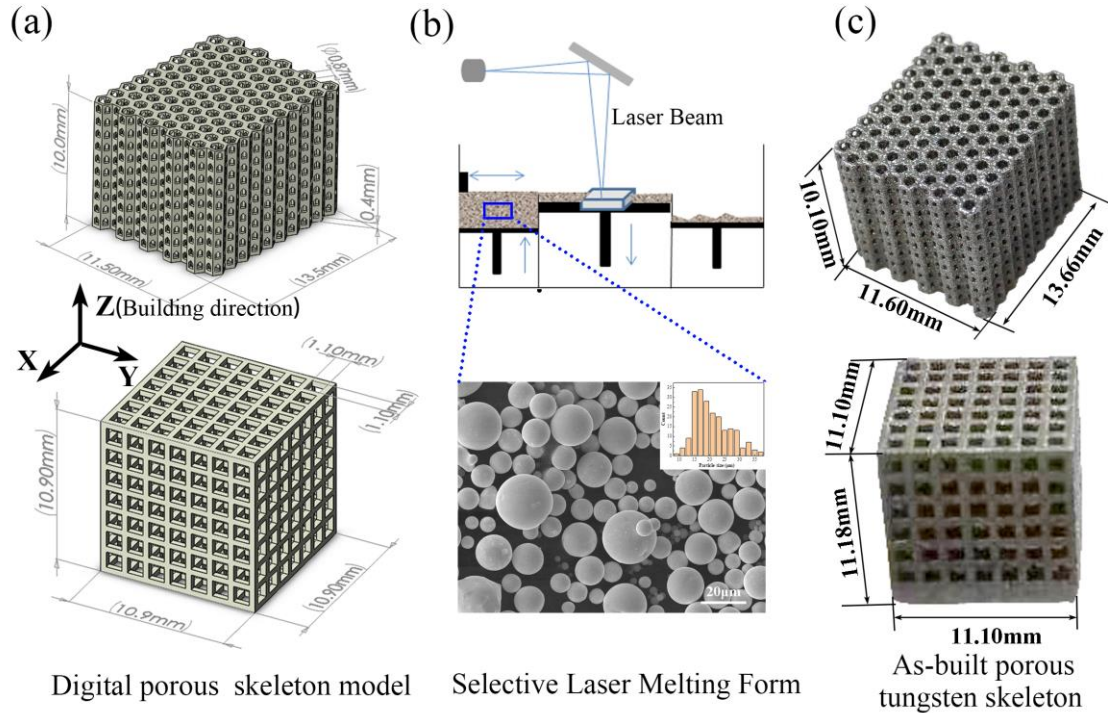
$$k = 1 - \frac{m_0}{V_0 \cdot \rho_w} \quad (2)$$

30 in which m_0 is the sample's weight in air, m_1 is its mass submerged in water, V_0 is the apparent
31 volume of sample, ρ_w is the density of pure tungsten (19.25g/cm³), ρ_{water} is water's density

1 (0.9960g/cm³) at 25°C.

2 Table 1 Composition of spherical tungsten powder (wt.%)

Element	W	C	O	N	P
Value (wt.%)	Balance	0.002	0.015	0.003	0.001



3

4 Figure 1 Structural designs and printing method of porous pure tungsten skeleton fabricated by SLM, (a) The
5 designed two types of porous skeletons; (b) Illustration of selective laser melting process; (c) Fabricated two
6 types of porous tungsten skeletons

7 3. Results and Discussion

8 XRD patterns of spherical tungsten powders and as-built tungsten skeletons are shown in
9 Figure 2. There are four diffraction peaks corresponding to (110), (200), (211), (310) planes of
10 tungsten crystals for both the powders and skeletons. However, compared to the pattern of raw
11 powder, that of the as-built tungsten skeleton shows much stronger and shaper diffraction peaks,
12 indicating an increased crystallinity. Meanwhile, there is no new tungsten phase formed after the
13 SLM process.

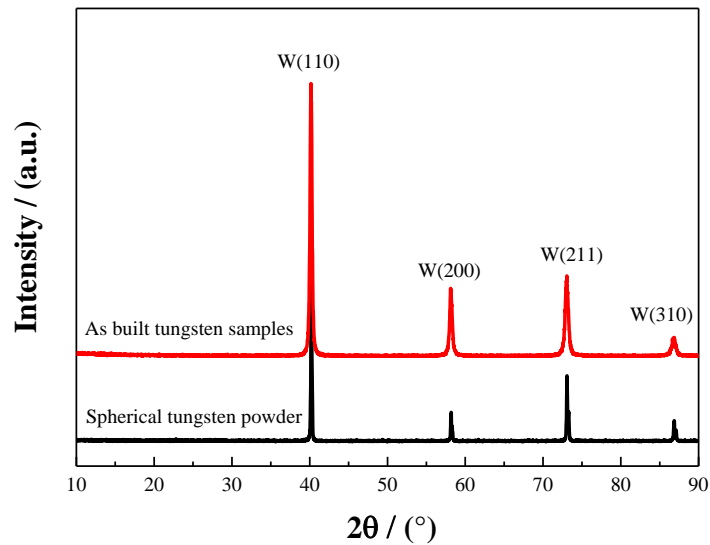
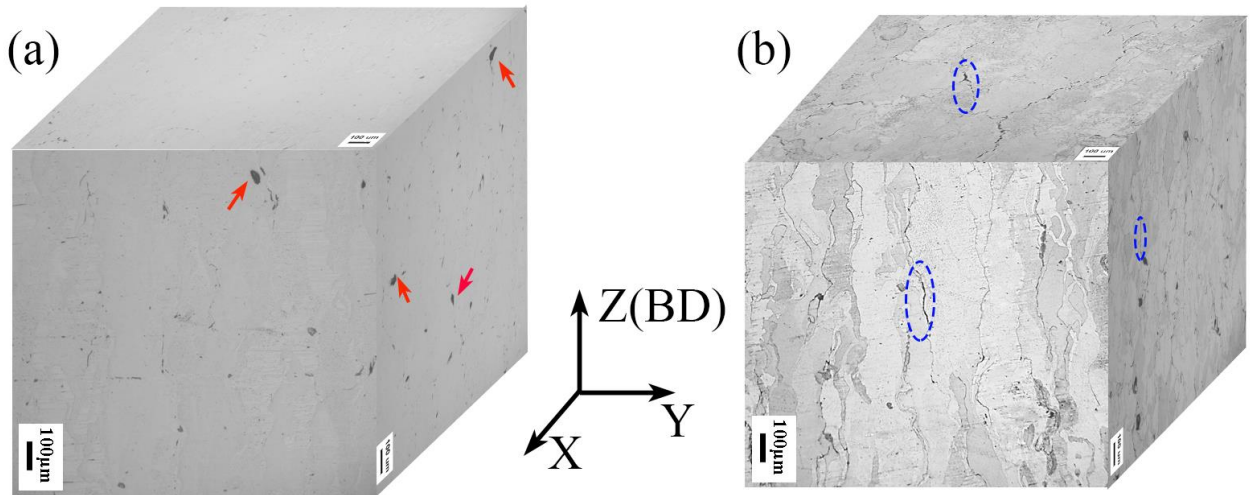


Figure 2 XRD pattern of raw tungsten powder and as built tungsten skeleton

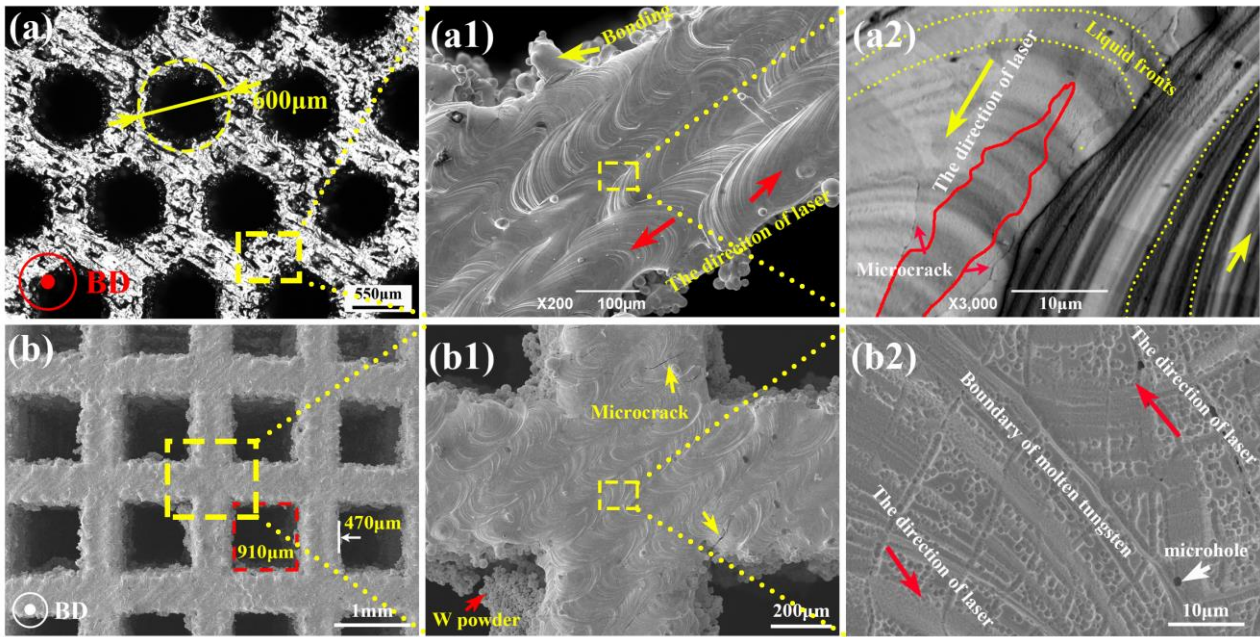
3.1 Microstructural analysis

Fig. 3 shows the optical images of as-built tungsten before and after chemical etching using a reagent of HF: HNO₃ (3:1 in a volume ratio). As shown in Fig. 3(a), there are a few micropores on the surface, which are mainly concentrated in the YZ/XZ plane (seen the red arrow). Those planes are the beginning and ending positions of laser beam scanning. Formations of these micro-pores is mainly because during laser beam scanning process, the protective gases were trapped inside the molten tungsten pool, and also large residual stress was generated due to the rapid cooling of the molten pool. Columnar grains and cracks (the blue zone in Figure 3(b)) along the Z axis direction can be observed on YZ/XZ planes of the as-fabricated tungsten, which has been chemically etched to reveal the structures. These cracks tend to grow along the grain boundaries [13], and are mainly caused by the rapid thermal shrinkage and large residual stress [16,17]. In the subsequent fabrication process, the heat-affected zone of laser molten pool is extended to the underlying layer [18], and the temperature gradient is very large along the Z axis, thus resulting in the formation of columnar grains. Whereas equiaxed crystals are formed along the XY plane.



1
2 Figure 3 Optical microscopy images of pure tungsten manufactured by SLM, (a) polished and before chemical
3 etching; (b) after chemical etching

4 Figure 4 shows SEM morphologies of the porous skeletons (for both the honeycomb one with
5 65% porosity and the square one with 80% porosity) along the XY plane. Figs. 4a and 4b show
6 that the as-built skeletons show similar pore shapes as the designed patterns. However, the average
7 pore size of skeletons is decreased compared to the designed ones (e.g., 890 μm and 1100 μm ,
8 respectively) because some tungsten powders were adhered along the edges of pores and the
9 junctions of scaffolds. In the laser scanning process, a large overlapping rate about 40% was
10 achieved. The laser beam was scanned in a zigzag pattern in the same plane, and the formed
11 scaffolds did not show obvious cracks and holes. The tungsten powders were sintered under the
12 heat-affected and hemispherical molten pool when the laser beam was applied [19]. The liquid
13 front and boundary of adjacent molten channels can be clearly observed as shown in Fig. 4a2.
14 There are a lot of micro-cracks at the grains boundaries as shown in Figs. 4a2 and 4b2, which are
15 mainly caused by the rapid thermal shrinkage of heat-affected zone in the laser molten pool.



1
2 Figure 4 Microstructure morphology of SLM pure skeletons along XY plane: (a) (a1) (a2) macro and selective
3 amplification zone image of 65% honey-comb skeleton; (b) (b1) (b2) macro and enlarged graphs of 80% square
4 skeleton
5

6 Figure 5 shows morphologies of skeletons along the YZ plane. Compared with those along
7 the XY plane, these skeleton structures show much rougher features, but they have well-defined
8 hole shapes without apparent macroscale defects. The rough surface is mainly caused by the
9 generation of sintered spherical powders which are trapped in the laser molten pool and many of
10 them are not fully melted [20]. The scale-like patterns can be observed at the starting/ending
11 positions of laser process. At a higher magnification (Fig. 5a2), microcracks with radial
12 distribution along the molten pool can be observed. For the SEM images of square skeletons (Fig.
13 5b), there is a significant overhanging under the horizontal scaffold which increases the size of
14 scaffold and reduces its porosity. During the laser beam scanning, in the first layer of horizontal
15 scaffold, there is whole powder support area below the scaffold. The laser molten pool is
16 immersed into this powder layer due to the capillary force. The enlarged molten pool causes
17 excessive melting of the powders under the scaffold [21,22]. The scale-like pattern can be
18 obviously seen in the vertical scaffold (Fig. 5b1). A small amount of micropores are found at the
19 interfaces of adjacent layers (Fig. 5b2). The possible reason is that some gasses are trapped during
20 the laser process.

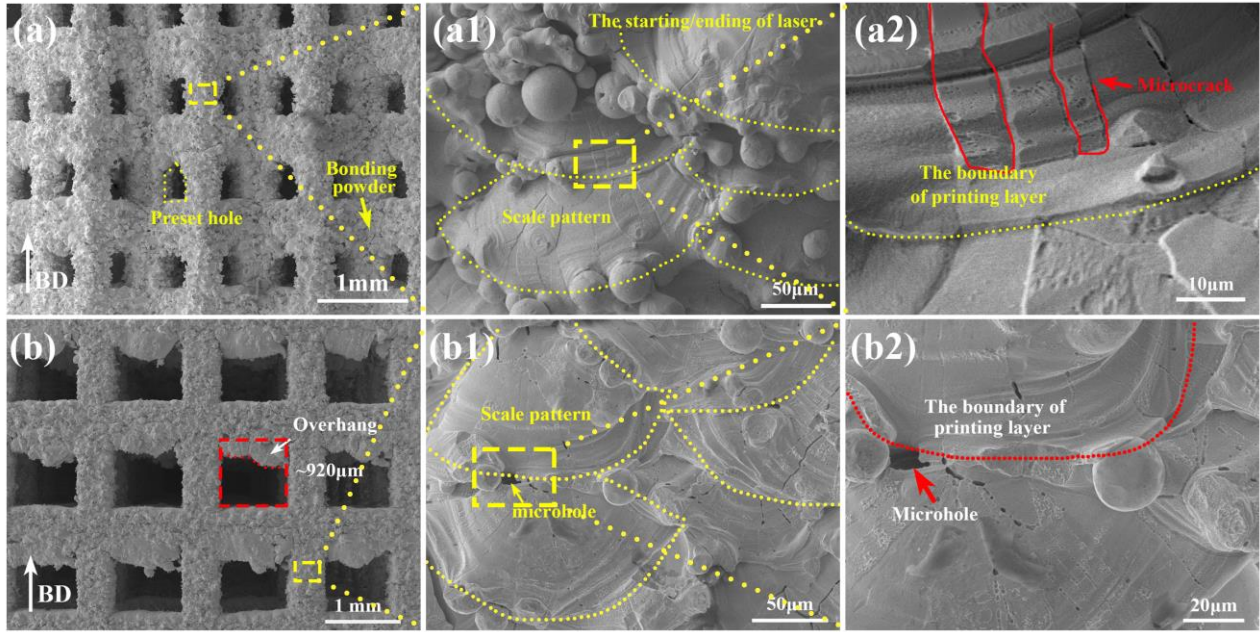


Figure 5 SLM porous tungsten microstructure morphology of YZ plane: (a) (a1) (a2) macro and partial amplification graph of 65% honeycomb skeleton; (b) (b1) (b2) low and high magnification of 80% square skeleton

Table 2 lists the measured porosities of all the samples. The relative density of tungsten obtained using a SLM method is $\sim 98.7\%$. The obtained density (18.99 g/cm^3) is lower than the theoretical density (19.25 g/cm^3) because of the formation of cracks and micro-pores during the laser scanning process, as shown in Fig. 3. However, the porosity of the porous tungsten skeleton is lower than the designed one. From the microscopic images of porous skeletons shown in Fig. 5b, there is overhanging phenomenon in the horizontal direction of scaffold and partially melted powders in the edge of scaffold, both of which decrease the porosity of the skeleton. References [21,23] also reported that the measured porosity is much lower than the designed one during the additive manufacturing of porous titanium base materials, which is consistent with the trend of porosity measurement in this work.

Table 2 The designed and measured porosities of different samples

Sample	Designed porosity	Measured porosity	Errors
0% solid cube	0%	1.3%	+1.3%
65% honeycomb	65%	51.8%	-13.2%
80% square	80%	67.8%	-12.2%

3.2 Mechanical properties

Compression properties of porous W skeletons were tested along both the Z axis and X axis (seen the inset in Fig. 6(a)). Fig. 6(a) shows stress-strain curves of different skeletons. The strength of 65% honeycomb skeleton is obviously anisotropic, e.g., the strength along the Z-axis is 256 MPa, whereas that along the X-axis is only 50 MPa. When compressed along the Z-axis of

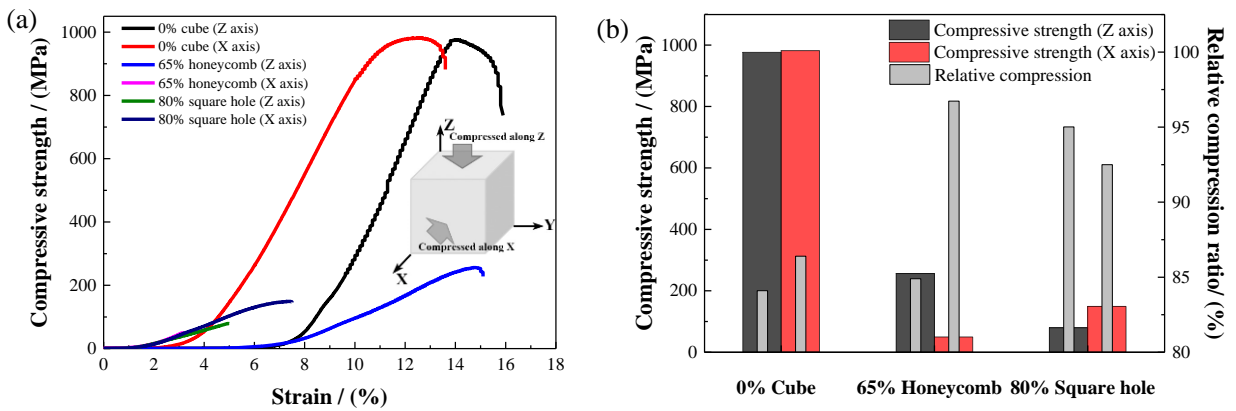
1 honeycomb skeleton structure, in which the cross-section morphology is alternatively hexagonal
 2 struts and uniform distributed scaffolds, the compressive stress is stably increased as shown in
 3 Fig. 6(a). Cross-section morphologies of the honeycomb skeletons along Z-axis and X-axis are
 4 quite different, thus causing these anisotropic properties.

5 The average value of compressive strength for the square skeleton is 149 MPa, which is
 6 consistent with the strength of square skeletons (with a porosity of $k=68\%$) prepared using a
 7 selective electron beam melting process reported in Ref. [24]. The square skeleton also exhibits an
 8 anisotropic behavior, mainly because the as-built sizes of horizontal and vertical scaffolds are
 9 different in the printing process. The overhanging phenomenon has significantly increased size of
 10 the horizontal struts (seen Fig. 5 (b)), and thus enhances the compressive strength in this direction.

11 Figure 6(b) compares the values of ultimate compressive strength and relative compressibility
 12 for a solid cube and two types of skeletons. The compressive strength values of the solid cube
 13 along X and Z directions are 982 and 976 MPa, respectively, which do not show significant
 14 differences. This proves that the anisotropy of skeleton is mainly caused by the formation of
 15 porous structures. The relative compression ratio (e_{ck}) of samples can be calculated using equation
 16 (3).

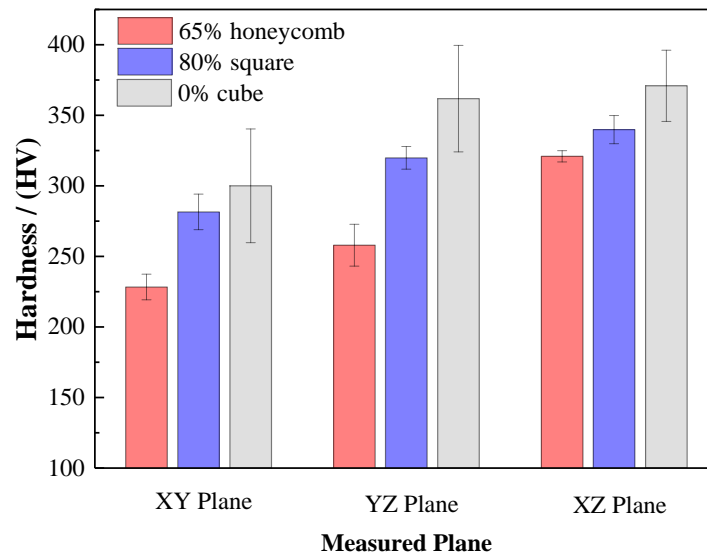
$$e_{ck} = (h_0 - h_k) / A_0 \times 100\% \quad (3)$$

17 where h_0 is the original height, and h_k is the height at fracture. The higher the relative compression
 18 ratio, the lower the strain. The higher relative compression ratio is linked with the less deformation
 19 of skeletons along compressive direction before fracture. The relative compression ratio of
 20 honeycomb skeletons also shows anisotropic behavior, e.g., 84% along Z axis and 96% along X
 21 direction, revealing that the compressive mechanisms of skeletons are different along the different
 22 directions.
 23



24
 25 Figure 6 The graph of compressive strength: (a) stress-strain curve of samples with different compressive
 26 direction; (b) Histogram of compressive strength and relative compression

1 Figure 7 shows the Vickers hardness values measured on different planes (e.g., XY, YZ, XZ)
 2 of the solid cube, 65% honeycomb and 80% square skeletons. It can be observed that the hardness
 3 values in the XY plane are lower than those in the other planes. There are two reasons to explain
 4 this trend. Firstly, the laser trace in the XY plane has a zigzag pattern, which generates a small
 5 temperature gradient. The scanning laser will cause partial melting of the as-formed layer, which
 6 releases the stress. [17]. Secondly, compared with the thermal gradient in the XY plane, that in the
 7 YZ/XZ plane is much larger. Because the adjacent area of laser starting/ending position is the
 8 powder area, the generated thermal stress cannot be easily released. The rapid cooling process
 9 results in a much higher hardness value along XZ plane. Clearly the hardness values are
 10 anisotropic along different planes after the laser selective melting process, which is caused by the
 11 different thermal gradients in each plane.

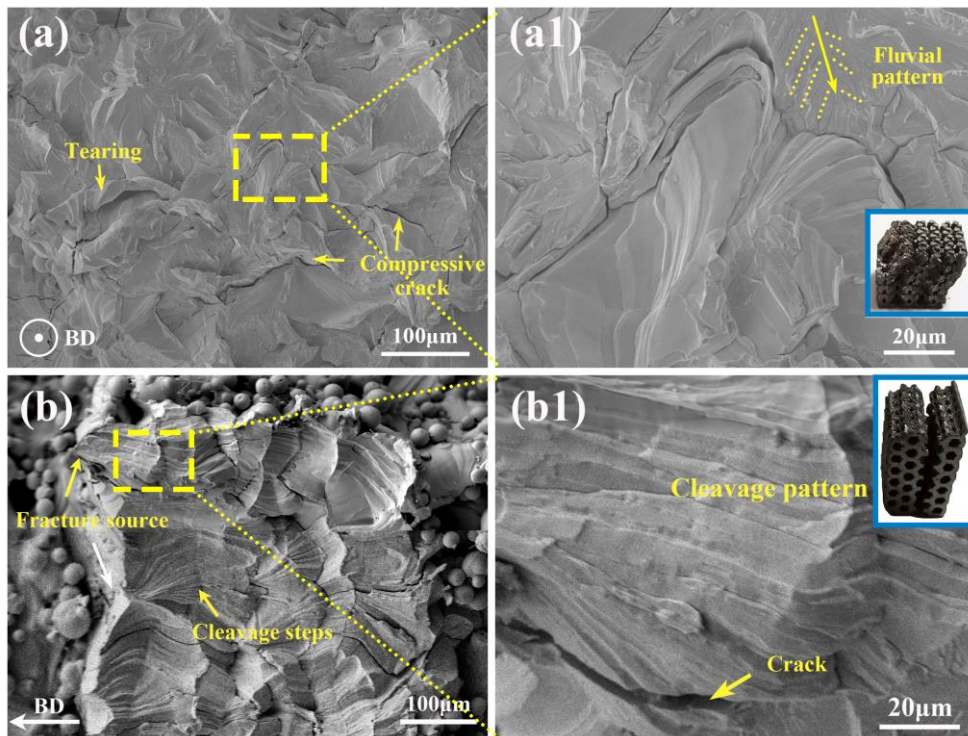


12
 13 Figure 7 Vickers hardness of as built skeletons in different planes

14 3.3 Fracture morphology analysis

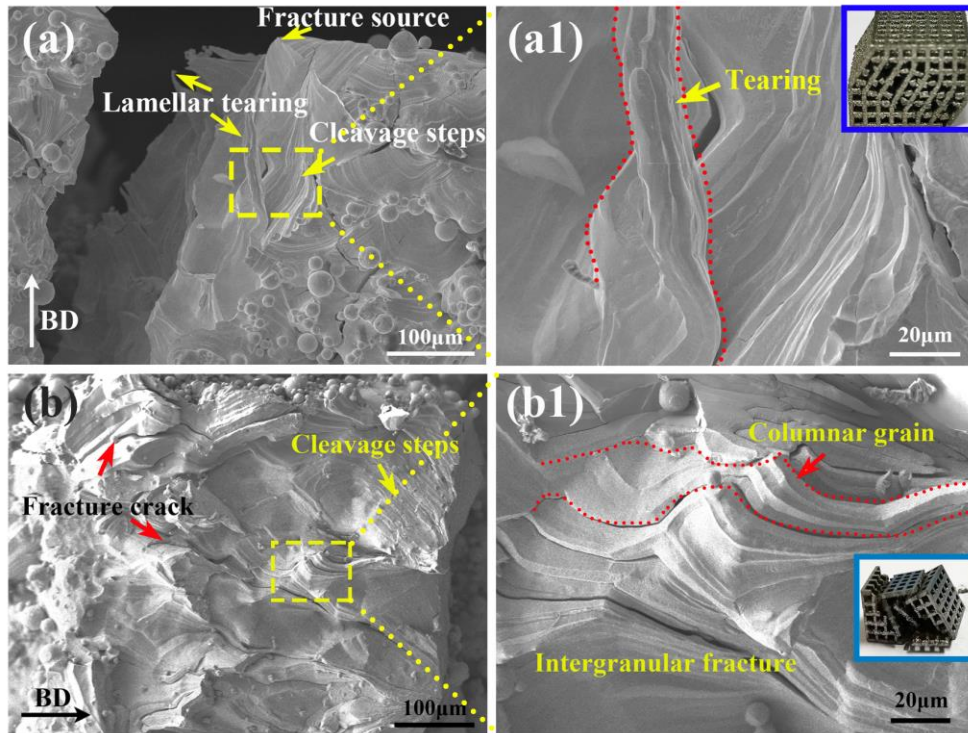
15 Figure 8 shows fracture morphologies of 65% porous honeycomb skeleton, which has been
 16 pressed along the Z axis and X axis, respectively. The fracture morphology shows a brittle fracture
 17 morphology, similar to those reported in Ref. [25]. Compared with the fracture morphology along
 18 the X-axis, that along the Z-axis shows transgranular fracture and severe tearing-like morphology.
 19 This is mainly because the columnar grains undergo severe extrusion and deformation before the
 20 final brittle fracture and the applied stress is perpendicular to the columnar grain direction.
 21 However, the fracture along the X direction appears to start from the middle of the horizontal
 22 scaffold, and there are no obvious tearing phenomenon and deformation of grain. This fracture
 23 morphology is a typical intergranular one with cleavage patterns. From the fracture photos (as
 24 shown in the insert images in Figure 8(a1)(b1)) and fracture morphologies in Figure 8(a)(b), the

1 deformation of grains along the Z axis is more severe than that along the X axis.



2
3 Figure 8 Fracture morphology of 65% honeycomb skeletons: (a) (b) compressed along Z axis; (c) (d)
4 compressed along X axis

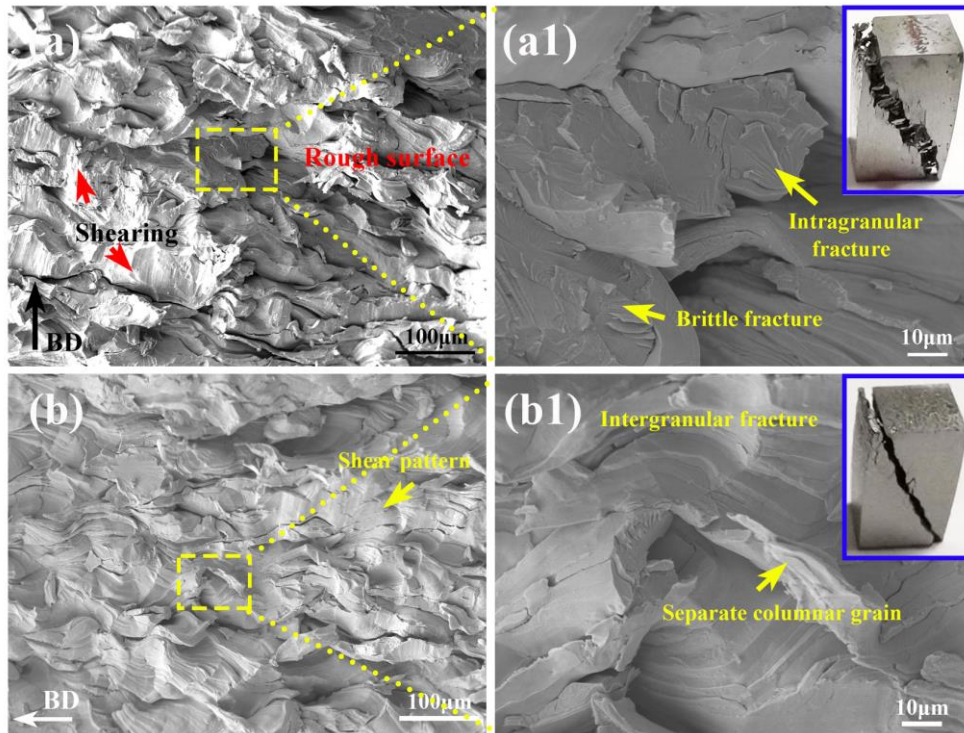
5 The fracture morphologies of square skeleton compressed along both the Z axis and X axis
6 reveal typical brittle fracture ones as shown in Fig. 9. From the image shown in Figs. 9(a) and (b),
7 with the increase of stress along the Z axis, we can observe that fracture occurs in the junction
8 between horizontal and vertical scaffolds, where a stress concentration is generated during the
9 compression process. When the skeleton is compressed along the Z axis, the twist angle of vertical
10 struct is about 30° . When compressed along the columnar crystals, the crystal grains are
11 perpendicular to the pressure direction. Meanwhile, when the horizontal and vertical scaffolds are
12 under compressive stress, the tendency and extent of deformations of Figs. 9(a1) and (b1) are quite
13 different [26]. When compressed in the X axis direction (Figs. 9c and 9d), the pressure is
14 perpendicular to the direction of columnar structures. The possibility of fracture occurring along
15 the grain boundaries is increased, thus the fracture surfaces present a typical intergranular fracture
16 morphology.



1

2 Figure 9 Fracture morphology of 80% square skeleton: (a) (b) compressed with the direction of Z axis, insert is
 3 the macro fracture image; (c) (d) compressed with the direction of X axis

4 Figures 10 shows the fracture morphologies of solid cube tungsten compressed along the Z
 5 axis and X axis, respectively. The fracture is along the diagonal direction of the block from the
 6 macroscopic image. Compared with the fracture surface compressed along the X axis, there are
 7 more obvious tearing morphology when compressed along the Z axis (shown in Fig.10a). When
 8 compressed along the Z axis, the angle between normal direction of the slip surface and the central
 9 axis of force is 90 degree. In this case, the stress is parallel to the direction of crystal grain. The
 10 crystals have been twisted, causing a brittle fracture (Fig. 10b, insert image). In the higher
 11 magnification image shown in Fig. 10b, brittle fracture can be clearly observed, including
 12 tearing-like and cleavage morphologies. A dense solid tungsten is a brittle material, and thus
 13 initiation and propagation of cracks are extremely fast, either through grain twisting/brittle fracture
 14 or intergranular fracture.

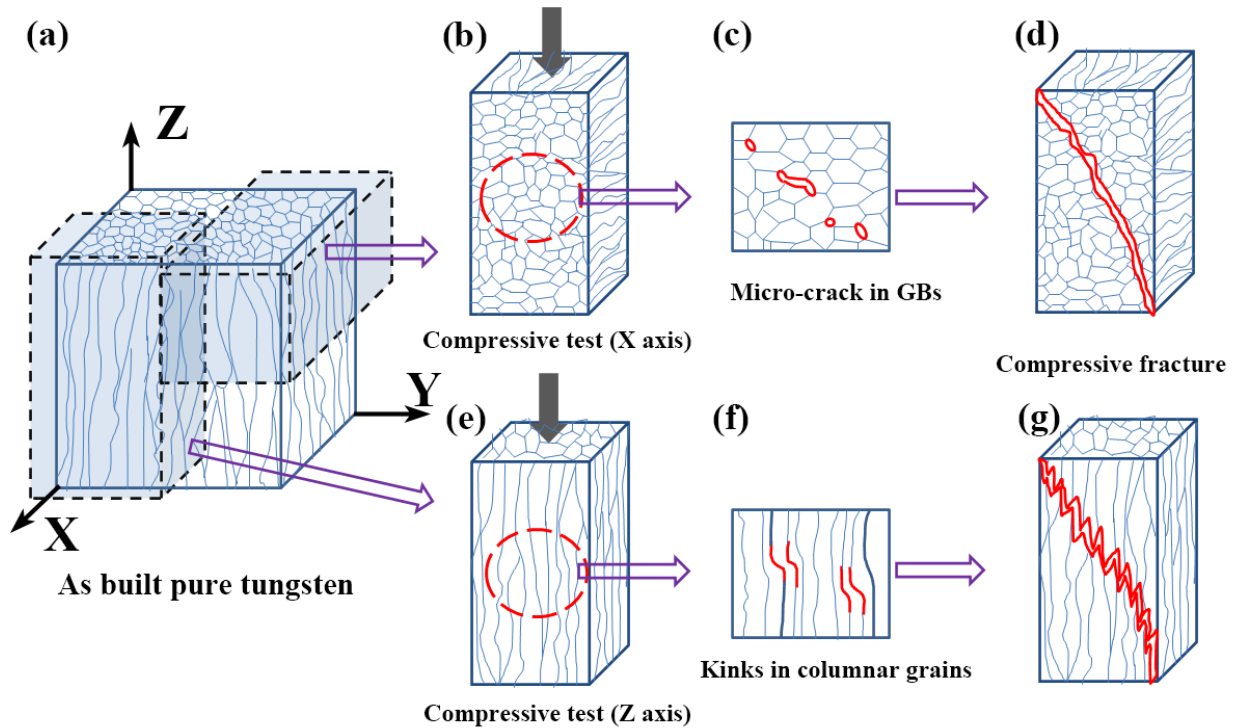


1

2 Figure 10 Compressive fracture morphology of cube tungsten: (a) (b) compressed along the Z axis, insert image;
 3 (c) (d) compressed along the X axis; Insert images are macro fracture

4 **3.4 Mechanisms of compressive fracture of porous skeleton**

5 Results clearly show that morphologies of the SLM processed samples along the Z axis and
 6 XY plane are quite different. The grains in the building direction show a columnar morphology.
 7 However, in the XY plane, grains show an equiaxial morphology. These different structures
 8 determine their fracture behaviors and fracture modes during the compression process [27,28].
 9 Figures 11 (b-d) schematically show the compression process of tungsten skeleton along the X axis.
 10 When compressed along this direction, the cracks appeared in XY plane are much smaller. The
 11 grains on the XY plane show an equiaxed crystal morphology. The fracture firstly appears at the
 12 grain boundaries. However, with the increase of pressure, microcracks appear between the
 13 adjacent gains, thus the cracks propagate along the grain boundaries thus forming intergranular
 14 fracture. Figures 11(e-g) schematically show the compression process along the Z direction. In this
 15 case, the grain growth direction is parallel to the Z axis. The rough macroscopic fracture appears in
 16 the YZ plane and the grains show a tearing-like and decohesion morphology. When the angle
 17 between the normal direction of the sliding surface and external force (F) is 90° , the grains stop to
 18 slip. However, if the stress applied to the grains is larger than the critical value, the partial bending
 19 of crystals and tearing will occur, and then the crack develops into a macroscopic fracture.



1

2 Figure 11 Schematic representation of compressive fracture process for the tungsten skeleton: (a) Gains
 3 topography of SLM ample; (b) Sampling along the X axis; (c) (d) (e) (f) (g)

4. Conclusion

5 Following conclusions can be obtained from this study:

6 (1) The porous skeletons with honeycomb and square shapes were successfully prepared
 7 using the LSM process. The skeletons have a porous structure with porosity values of 52 vol.%
 8 (honeycomb), 68 vol.% (square), and their compressive strengths are 256 MPa and 149 MPa,
 9 respectively. The hardness of a dense cube on XZ plane is higher than XY plane, and the
 10 maximum difference is 70.9 HV.

11 (2) In the SLM processed porous tungsten samples, the grains present an equiaxed
 12 morphology in the XY plane, and a columnar morphology (parallel to the Z axis) in the YZ/XZ
 13 plane. The overlapping rate between adjacent laser channels (XY plane) is about 40%. In the YZ
 14 plane, the scale morphology of superimposed laser channels can be clearly observed.

15 (3) The fracture mechanism is determined by the columnar crystals along the Z axis of the
 16 SLM samples. When compressed along the Z axis, some columnar crystals will show transgranular
 17 fracture, then microcracks are formed thus leading to the fracture with a rough morphology. When
 18 compressed along the X axis, the deflection of cracks occurs between adjacent crystal grains, and
 19 the fracture morphology is a typically intergranular fracture.

Acknowledgements

The authors would like to acknowledge the financial supports from Xi'an Science Research Project of China (No. 2020KJRC0089) and Shaanxi Coal Industry Group United Fund of China (No.2019JLM-2), Shaanxi Key Research and Development Plan of China(2019GY-188), National Natural Science Foundation of China (No.51901192), and Electrical Materials and Infiltration Key Laboratory of Shaanxi Province, and International Exchange Grant (IEC/NSFC/201078) through Royal Society UK and the National Natural Science Foundation of China, and Royal academy of Engineering UK-Research Exchange with China and India.

References

- [1] A. V. Müller, G. Schlick, R. Neu, C. Anstatt, T. Klimkait, J. Lee, B. Pascher, M. Schmitt, C. Seidel, Additive manufacturing of pure tungsten by means of selective laser beam melting with substrate preheating temperatures up to 1000 ° C, *Nucl. Mater. Energy*. (2019). <https://doi.org/10.1016/j.nme.2019.02.034>.
- [2] D. Dorow-Gerspach, A. Kirchner, T. Loewenhoff, G. Pintsuk, T. Weißgärber, M. Wirtz, Additive manufacturing of high density pure tungsten by electron beam melting, *Nucl. Mater. Energy*. 28 (2021). <https://doi.org/10.1016/j.nme.2021.101046>.
- [3] W. Chen, Y. Shi, L. Dong, L. Wang, H. Li, Y. Fu, Infiltration sintering of WCu alloys from copper-coated tungsten composite powders for superior mechanical properties and arc-ablation resistance, *J. Alloys Compd.* (2017). <https://doi.org/10.1016/j.jallcom.2017.08.164>.
- [4] J.W. Coenen, Y. Mao, S. Sistla, J. Riesch, T. Hoeschen, C. Broeckmann, R. Neu, C. Linsmeier, Improved pseudo-ductile behavior of powder metallurgical tungsten short fiber-reinforced tungsten (Wf/W), *Nucl. Mater. Energy*. (2018). <https://doi.org/10.1016/j.nme.2018.05.001>.
- [5] D. Terentyev, M. Vilémová, C. Yin, J. Veverka, A. Dubinko, J. Matějčíček, Assessment of mechanical properties of SPS-produced tungsten including effect of neutron irradiation, *Int. J. Refract. Met. Hard Mater.* (2020). <https://doi.org/10.1016/j.ijrmhm.2020.105207>.
- [6] H. Noto, Y. Hishinuma, T. Muroga, H. Benoki, Microstructure and mechanical properties of dispersion strengthened tungsten by HIP treatment followed by thermal annealing, *Results Mater.* (2020). <https://doi.org/10.1016/j.rinma.2020.100116>.
- [7] F. Scalzo, G. Totis, E. Vaglio, M. Sortino, Experimental study on the high-damping properties of metallic lattice structures obtained from SLM, *Precis. Eng.* 71 (2021) 63–77. <https://doi.org/10.1016/j.precisioneng.2021.02.010>.
- [8] A.T. Sidambe, Y. Tian, P.B. Prangnell, P. Fox, Effect of processing parameters on the densification, microstructure and crystallographic texture during the laser powder bed fusion of pure tungsten, *Int. J. Refract. Met. Hard Mater.* (2019). <https://doi.org/10.1016/j.ijrmhm.2018.10.004>.
- [9] K. Li, G. Ma, L. Xing, Y. Wang, C. Yu, J. Chen, J. Ma, G. Wu, W. Liu, Z. Shen, X. Huang, Crack suppression via in-situ oxidation in additively manufactured W-Ta alloy, *Mater. Lett.* (2020). <https://doi.org/10.1016/j.matlet.2019.127212>.
- [10] T. Maconachie, M. Leary, B. Lozanovski, X. Zhang, M. Qian, O. Faruque, M. Brandt, SLM lattice structures: Properties, performance, applications and challenges, *Mater. Des.* (2019).

<https://doi.org/10.1016/j.matdes.2019.108137>.

- [11] D. Wang, Z. Wang, K. Li, J. Ma, W. Liu, Z. Shen, Cracking in laser additively manufactured W: Initiation mechanism and a suppression approach by alloying, *Mater. Des.* 162 (2019) 384–393. <https://doi.org/10.1016/j.matdes.2018.12.010>.
- [12] X. Ren, H. Liu, F. Lu, L. Huang, X. Yi, Effects of processing parameters on the densification, microstructure and mechanical properties of pure tungsten fabricated by optimized selective laser melting: From single and multiple scan tracks to bulk parts, *Int. J. Refract. Met. Hard Mater.* 96 (2021) 105490. <https://doi.org/10.1016/j.ijrmhm.2021.105490>.
- [13] Z. Hu, Y. Zhao, K. Guan, Z. Wang, Z. Ma, Pure tungsten and oxide dispersion strengthened tungsten manufactured by selective laser melting: Microstructure and cracking mechanism, *Addit. Manuf.* 36 (2020) 101579. <https://doi.org/10.1016/j.addma.2020.101579>.
- [14] M. Guo, D. Gu, L. Xi, H. Zhang, J. Zhang, J. Yang, R. Wang, Selective laser melting additive manufacturing of pure tungsten: Role of volumetric energy density on densification, microstructure and mechanical properties, *Int. J. Refract. Met. Hard Mater.* 84 (2019) 105025. <https://doi.org/10.1016/j.ijrmhm.2019.105025>.
- [15] S. Wen, C. Wang, Y. Zhou, L. Duan, Q. Wei, S. Yang, Y. Shi, High-density tungsten fabricated by selective laser melting: Densification, microstructure, mechanical and thermal performance, *Opt. Laser Technol.* (2019). <https://doi.org/10.1016/j.optlastec.2019.03.018>.
- [16] B. Vrancken, R.K. Ganeriwala, M.J. Matthews, Analysis of laser-induced microcracking in tungsten under additive manufacturing conditions: Experiment and simulation, *Acta Mater.* 194 (2020) 464–472. <https://doi.org/10.1016/j.actamat.2020.04.060>.
- [17] P. Mercelis, J.P. Kruth, Residual stresses in selective laser sintering and selective laser melting, *Rapid Prototyp. J.* (2006). <https://doi.org/10.1108/13552540610707013>.
- [18] S. Raghavendra, A. Molinari, V. Fontanari, V. Luchin, G. Zappini, M. Benedetti, F. Johansson, J. Klarin, Tensile and compression properties of variously arranged porous Ti-6Al-4V additively manufactured structures via SLM, in: *Procedia Struct. Integr.*, 2018. <https://doi.org/10.1016/j.prostr.2018.12.025>.
- [19] Z.C. Fang, Z.L. Wu, C.G. Huang, C.W. Wu, Review on residual stress in selective laser melting additive manufacturing of alloy parts, *Opt. Laser Technol.* 129 (2020) 106283. <https://doi.org/10.1016/j.optlastec.2020.106283>.
- [20] E. Sallica-Leva, A.L. Jardini, J.B. Fogagnolo, Microstructure and mechanical behavior of porous Ti-6Al-4V parts obtained by selective laser melting, *J. Mech. Behav. Biomed. Mater.* (2013). <https://doi.org/10.1016/j.jmbbm.2013.05.011>.
- [21] Q. Ran, W. Yang, Y. Hu, X. Shen, Y. Yu, Y. Xiang, K. Cai, Osteogenesis of 3D printed porous Ti6Al4V implants with different pore sizes, *J. Mech. Behav. Biomed. Mater.* (2018).

<https://doi.org/10.1016/j.jmbbm.2018.04.010>.

- [22] X. Zhou, X. Liu, D. Zhang, Z. Shen, W. Liu, Balling phenomena in selective laser melted tungsten, *J. Mater. Process. Technol.* 222 (2015) 33–42.
<https://doi.org/10.1016/j.jmatprotec.2015.02.032>.
- [23] K. Refai, C. Brugger, M. Montemurro, N. Saintier, An experimental and numerical study of the high cycle multiaxial fatigue strength of titanium lattice structures produced by Selective Laser Melting (SLM), *Int. J. Fatigue.* (2020). <https://doi.org/10.1016/j.ijfatigue.2020.105623>.
- [24] G. Yang, N. Liu, L. Jia, Z. Xu, K. Yang, H. Liu, H. Tang, Fabrication and compression property of tungsten skeleton for tungsten-copper composite, *Fenmo Yejin Cailiao Kexue Yu Gongcheng/Materials Sci. Eng. Powder Metall.* (2017).
- [25] A.M. Lennon, K.T. Ramesh, The thermoviscoplastic response of polycrystalline tungsten in compression, *Mater. Sci. Eng. A.* (2000). [https://doi.org/10.1016/S0921-5093\(99\)00517-1](https://doi.org/10.1016/S0921-5093(99)00517-1).
- [26] C. Chang, J. Huang, X. Yan, Q. Li, M. Liu, S. Deng, J. Gardan, R. Bolot, M. Chemkhi, H. Liao, Microstructure and mechanical deformation behavior of selective laser melted Ti6Al4V ELI alloy porous structures, *Mater. Lett.* (2020).
<https://doi.org/10.1016/j.matlet.2020.128366>.
- [27] Y. Zhou, X. Zeng, Z. Yang, H. Wu, Effect of crystallographic textures on thermal anisotropy of selective laser melted Cu-2.4Ni-0.7Si alloy, *J. Alloys Compd.* (2018).
<https://doi.org/10.1016/j.jallcom.2018.01.335>.
- [28] I.A. Ovid'ko, R.Z. Valiev, Y.T. Zhu, Review on superior strength and enhanced ductility of metallic nanomaterials, *Prog. Mater. Sci.* (2018).
<https://doi.org/10.1016/j.pmatsci.2018.02.002>.